

# Northumbria Research Link

Citation: Cai, Sheng-Xun, Song, Xian-Qiang, Chi, Zong-Tao, Fu, Yong Qing, Fang, Zheng-Tao, Geng, Sun-Ying-Yue, Kang, Ya-Ru, Yang, Xiao-Xu, Qin, Jian-Feng and Xie, Wan-Feng (2021) Rational design of Bi-doped rGO/Co3O4 nanohybrids for ethanol sensing. Sensors and Actuators B: Chemical, 343. p. 130118. ISSN 0925-4005

Published by: Elsevier

URL: <https://doi.org/10.1016/j.snb.2021.130118>  
<<https://doi.org/10.1016/j.snb.2021.130118>>

This version was downloaded from Northumbria Research Link:  
<http://nrl.northumbria.ac.uk/id/eprint/46368/>

Northumbria University has developed Northumbria Research Link (NRL) to enable users to access the University's research output. Copyright © and moral rights for items on NRL are retained by the individual author(s) and/or other copyright owners. Single copies of full items can be reproduced, displayed or performed, and given to third parties in any format or medium for personal research or study, educational, or not-for-profit purposes without prior permission or charge, provided the authors, title and full bibliographic details are given, as well as a hyperlink and/or URL to the original metadata page. The content must not be changed in any way. Full items must not be sold commercially in any format or medium without formal permission of the copyright holder. The full policy is available online: <http://nrl.northumbria.ac.uk/policies.html>

This document may differ from the final, published version of the research and has been made available online in accordance with publisher policies. To read and/or cite from the published version of the research, please visit the publisher's website (a subscription may be required.)

# Rational design of Bi-doped rGO/Co<sub>3</sub>O<sub>4</sub> nanohybrids for ethanol sensing

Sheng-Xun Cai <sup>a†</sup>, Xian-Qiang Song <sup>a†</sup>, Zong-Tao Chi <sup>a</sup>, Yong-Qing Fu <sup>b</sup>, Zheng-Tao Fang <sup>a</sup>, Sun-Ying-Yue Geng <sup>a</sup>,  
Ya-Ru Kang <sup>a</sup>, Xiao-Xu Yang <sup>a</sup>, Jian-Feng Qin <sup>c</sup>, Wan-Feng Xie <sup>a\*</sup>

<sup>a</sup> School of Electronics & Information, State Key Laboratory of Bio-Fibers and Eco-Textiles, Qingdao University,  
Qingdao 266071, China

<sup>b</sup> Faculty of Engineering and Environment, Northumbria University, Newcastle upon Tyne NE1 8ST, UK

<sup>c</sup> Qingdao Open University, Qingdao 266071, China

\* To whom correspondence should be referred.

Wan-Feng Xie: [wfxie@qdu.edu.cn](mailto:wfxie@qdu.edu.cn)

## Abstract

Gas sensors based on metal oxide semiconductors (MOSCs) and reduced graphene oxide (rGO) for sensing of organic volatile compounds often suffer from high operation temperature, low responses, poor selectivity, or narrow detection range. Herein, we design and fabricate Bi-doped rGO/Co<sub>3</sub>O<sub>4</sub> (BGCO) nanohybrids with a flower morphology, which have been applied as a sensing layer for an ethanol sensor. This BGCO sensor exhibits a maximum *p*-type response of 178.1 towards 500 ppm ethanol at an optimum working temperature of 120 °C. The sensor's detection range for the ethanol concentration is from 500 ppb to 500 ppm, and the sensor has an excellent selectivity to ethanol compared to other types of organic volatile gases and oxidizing gas such as NO<sub>2</sub>. The enhanced ethanol sensing mechanism is attributed to the increased conductivity of Bi doped rGO/Co<sub>3</sub>O<sub>4</sub> material. Additionally, incorporation of Bi dopant can promote the redox reaction, and the MOSCs act as the catalyst.

**Keywords:** semiconducting metal oxide, rGO, Bi doped Co<sub>3</sub>O<sub>4</sub>, ethanol sensor, resistive sensor

## 1. Introduction

With the rapid development of Internet of things, various sensor-based techniques are being extensively developed and applied for industry, agriculture, environment control, enhancement of life quality, and safety [1-4]. Among various types of sensors, chemiresistive gas sensors based on metal oxide semiconductors (MOSCs), such as  $\text{Co}_3\text{O}_4$  [5],  $\text{rGO}/\text{Co}_3\text{O}_4$  [6-8],  $\text{Bi}_2\text{O}_3$  [9],  $\text{SnO}_2$  [10],  $\text{In}_2\text{O}_3$  [11], and  $\text{WO}_3$  [12,13], as well as their nanocomposites [14-16], have many advantages including good sensitivity, selectivity, stability, cost effectiveness, and simple implementation for real-time control. All of these make them competitive for usages in environmental monitoring, food safety, industrial production, and disease diagnosis [17-19].

Volatile organic compounds (VOCs), including ethanol ( $\text{C}_2\text{H}_6\text{O}$ ), formaldehyde ( $\text{CH}_2\text{O}$ ), toluene ( $\text{C}_7\text{H}_8$ ), methanol ( $\text{CH}_3\text{OH}$ ), ethylene glycol ( $((\text{CH}_2\text{OH})_2)$ ) and other aromatic carbohydrates, are hazardous to human health and can cause irritation of mucous membranes and upper respiratory tracts [20,21]. Nevertheless, our olfactory system is insensitive to accurately detect these types of harmful gases. Therefore, it is critical to develop high performance gas sensors not only for detection of toxic, explosive or flammable vapors (which could come from free emissions or destructive leakage), but also for quality or concentration control of living conditions, traffic routine inspections, rapid disease diagnosis and food inspection [22]. Ethanol ( $\text{CH}_3\text{CH}_2\text{OH}$ ), for example, is one of the important VOCs used in food, biological and brewing industries. In recent years, studies for gas sensors for ethanol have been increased rapidly due to their extensive applications such as drunken-driving monitoring, safety tests for food package, and leakage detection in chemical factories [23,24]. Large quantity leakage or evaporation of ethanol may induce risk of explosion in brewery houses or storehouses [25]. Therefore, it is critically required for ethanol sensors with low operating temperature, fast detection, high sensitivity, and good selectivity.

The key working mechanism of these MOSCs based gas sensors is that the target gas molecules are chemisorbed and react with the oxygen species such as  $\text{O}^-$ ,  $\text{O}_2^-$ ,  $\text{O}^{2-}$  on the surface of the sensing material, which leads to changes of device's properties such

as electrical resistance [8,17]. To further enhance the gas sensing performance including low working temperature, sensitivity, selectivity, stability, and reproducibility, different strategies have been developed [26]. For example, doping of these MOSCs have been extensively studied to enhance the synergistic effects of the binary/ternary metal oxide materials ( $\text{Bi}_2\text{O}_3$ ,  $\text{SnO}_2$ ,  $\text{MoO}_3$  and  $\text{Co}_3\text{O}_4$ ) and increase the surface chemical states of the electrons and high surface-to-volume ratios [27]. Heterostructures have also been widely used, including  $n$ - $n$ ,  $p$ - $p$  and  $p$ - $n$  junctions, where  $p$  is  $p$ -type semiconductor,  $n$  refers to  $n$ -type semiconductor. Many studies also applied composites of the MOSCs, for example, with the reduced graphene oxide (rGO), which can manipulate the Fermi energy level and large specific surface area [28-30].

Recently, there are studies reported using  $\text{Zn}_{1-x}\text{Fe}_x\text{O}/\text{rGO}$  [31],  $\text{SnO}_2\text{-rGO}$  [32],  $\text{rGO-CuO}$  [33] and  $\text{MoO}_3\text{-rGO}$  [34] nanocomposites for the ethanol sensors. However,  $\text{rGO}/\text{Co}_3\text{O}_4$  [35],  $\text{Co}_3\text{O}_4/\text{N-doped rGO}$  nanocomposites [8], and rGO decorated hollow  $\text{Co}_3\text{O}_4$  nano/microspheres [7], are still deserved to be further investigated due to their low responses and high operating temperatures. For instance, Liu's group synthesized rGO decorated hollow  $\text{Co}_3\text{O}_4$  spheres using a solvothermal method and then applied them into an ethanol sensor. The sensor showed a  $p$ -type sensing behavior, and the response value is 13.5 towards 100 ppm ethanol, which is 3.7 times higher than that of the pure  $\text{Co}_3\text{O}_4$  [35]. In 2019, Sun's group fabricated  $\text{Co}_3\text{O}_4$  and rGO nanosheets, which have been used for ethanol sensing. They reported that the nanocomposite with 15 wt% of rGO has the best sensitivity when operated at 200 °C [7]. In 2020, Lin and co-workers reported that  $\text{Co}_3\text{O}_4/\text{N-doped rGO}$  nanocomposite with a mesoporous structure exhibited a  $p$ -type response for ethanol which can be operated at 200 °C [8].

In very recent years, various  $\text{rGO}/\text{Co}_3\text{O}_4$  nanocomposites have been extensively studied as the ethanol sensing materials. However, the sensor's performance such as sensitivity, working temperature and selectivity of the  $\text{rGO}/\text{Co}_3\text{O}_4$  based sensors is far from satisfactory, owing to their relatively high intrinsic resistance. One alternative strategy for enhancing sensing properties is to introduce other components (e.g., Bi, Zr, Ag) [36-38], especially for those elements with a high electronegativity. These elements can have a synergistic effect with Co to modulate the surface states, reactant adsorption,

and activation. According to the literature, the electronegativity of Bi is 1.9, which is beneficial in gas sensing because it is known to promote electron transfer [39]. In addition, the conductivity of Bi doped rGO/Co<sub>3</sub>O<sub>4</sub> might be greatly improved because of the mismatch of lattice constants [40], which was induced by the doped Bi, because the radius of Bi atoms is larger than that of Co atoms. However, to the best of our knowledge, there are few reports on the ethanol sensing using Bi-doped rGO/Co<sub>3</sub>O<sub>4</sub> nanohybrids. Therefore, in the present investigation, Bi-doped rGO/Co<sub>3</sub>O<sub>4</sub> nanohybrids have been synthesized via one-pot solvent-thermal method. Based on this design methodology, we found that incorporation of 1% Bi (mass ratio) into rGO/Co<sub>3</sub>O<sub>4</sub> nanohybrid can enhance the ethanol sensing performance (e.g., response and selectivity) significantly.

## 2. Experimental

### 2.1 Preparation of Bi-doped rGO/Co<sub>3</sub>O<sub>4</sub> nanocomposite

All analytical grade reagents and chemicals were purchased from Aladdin (Shanghai, China), and used as received without any further purification. Mixtures of 747.2 mg Co(Ac)<sub>2</sub>·4H<sub>2</sub>O, 7.472 mg Bi(NO<sub>3</sub>)<sub>3</sub>·5H<sub>2</sub>O, 500 mg 1,3,5 Trimesic acid (C<sub>9</sub>H<sub>6</sub>O<sub>6</sub>), and 300 mg ammonium fluoride (NH<sub>4</sub>F) were dissolved into the 40 ml absolute ethyl alcohol, and obtained a solution A. Graphene oxide (GO) nanosheets were synthesized from the natural graphite via the modified Hummers method, and then ultrasonically dispersed into 10 ml absolute ethyl alcohol at 250 W for 2 h, which obtained a solution B. Successively, the solutions of A and B were transferred into a 50 ml autoclave and heated at 180 °C for 24 h. The obtained products were centrifugated and washed with ethanol and water for 3 times, and dried at 80 °C for 12 h. The dark violet colored precursor was changed into black powder after calcination at 300 °C for 2 h. According to the mass ratio of Co(Ac)<sub>2</sub>·4H<sub>2</sub>O and Bi(NO<sub>3</sub>)<sub>3</sub>·5H<sub>2</sub>O, the prepared Bi-doped rGO/Co<sub>3</sub>O<sub>4</sub> nanocomposite was denoted as 1%BGCO. Similarly, we prepared other three samples via changing the weight of Bi(NO<sub>3</sub>)<sub>3</sub>·5H<sub>2</sub>O from 0 mg (0%), 22.416 mg (3%), to 44.832 mg (6%), and named them as 0%BGCO, 3%BGCO, and 6%BGCO, respectively.

## 2.2 Preparation of gas sensing set-up

In the typical sensor fabrication process, 100 mg 0%BGO, 1%BGO, 3%BGO, 6%BGO nanocomposites were mixed with *N, N*-dimethylformamide (DMF) to form paste, respectively. The paste was then drop-coated onto the surface of a ceramic tube with four platinum (Pt) electrodes to form a uniform coating. The coated ceramic tube with the BGO were welded to a special six-polar pedestal. Finally, a Ni–Cr heating coil was inserted into the coated ceramic tube for heating purposes. The gas sensing performance was characterized using a gas sensing system (MA1.0, Narui Electronics Co. Ltd., China). The sensing response was calculated by the resistance ratio of the sensor resistance in sensing gases ( $R_g$ ) to that in fresh air ( $R_a$ ). The response time was defined as the time taken for the 90%-fold resistance alteration of gas sensors in the adsorption processes, whereas the recovery time was defined as the period taken by sensing device to reach 90% of its initial resistance after the exposed to air [41].

## 2.3 Materials Characterization

X-ray diffraction (XRD) patterns of the composites were obtained using a Bruker AXS (D8, advance, Cu  $K\alpha$  X-ray source) diffractometer at a scanning rate of  $1^\circ \text{ min}^{-1}$ . The morphologies of the samples were investigated using a field emission scanning electron microscope (FE-SEM, Zeiss Gemini 500) and a high resolution transmission electron microscope (HR-TEM, JEOL-2100F 200 kV). The elemental mapping of the samples was performed using an energy dispersive X-ray spectroscope (EDX, Oxford Link-ISIS 300) at 15 kV. The spectra of X-ray photoelectron spectroscope (XPS) were recorded using a Thermo Scientific Escalab 250xi instrument equipped with a monochromatic Al  $K\alpha$  source. The specific surface areas were determined by BET measurements (Autosorb iQ Station 1, USA). Experiments using ultraviolet photoelectron spectroscopy (UPS, Thermo Fisher Scientific Co.) was carried out in ultrahigh-vacuum environment with He I ( $h\nu = 21.2 \text{ eV}$ ).

## 3. Results and discussion

Fig. 1a presents the synthesis process of the BGO sensing materials. Here, the BGO nanohybrids were obtained via one-pot solvent-thermal method. Fig. 1b shows the surface morphologies and microstructures of the nanocomposite of Bi-doped

rGO/Co<sub>3</sub>O<sub>4</sub> obtained using the FE-SEM. The surface of 1%BGCO composite shows a flower-type morphology, and the lamellar structure of rGO could hardly be seen as the substrate for the nucleation and growth of Co<sub>3</sub>O<sub>4</sub>. The surface also shows interconnected pores, and the pore diameter is ranged from several nanometers to several micrometers (Fig. 1c), which is consistent with the structure of the rGO [42]. Fig. 1d shows a TEM image, revealing the Co<sub>3</sub>O<sub>4</sub> on the translucent layer of rGO [43]. Fig. 1e shows a HR-TEM image of the sample, where the two lattice fringes with spacings of 0.47 nm and 0.24 nm are identified as the (111) and (311) lattice planes of hexagonal Co<sub>3</sub>O<sub>4</sub> [44,8]. To elucidate the elemental composition of the 1%BGCO nanohybrids, EDX elemental mapping was performed (Fig. 1f to i), and the results confirm that the sample of 1%BGCO contain C (Fig. 1f), O (Fig. 1g), Co (Fig. 1h) and Bi (Fig. 1i), evenly distributed within the selected area. On the other hand, Bi elements are sparsely scattered on the surface of 1%BGCO.

**Fig. 1.** (a) Illustration of the synthesis process of flower shaped Bi-doped rGO/Co<sub>3</sub>O<sub>4</sub> nanohybrids; (b) low-magnification SEM and (c) high-magnification SEM of Bi-doped rGO/Co<sub>3</sub>O<sub>4</sub> nanohybrids; (d) low-magnification TEM and (e) HR-TEM image of Bi-doped rGO/Co<sub>3</sub>O<sub>4</sub> nanohybrids; the corresponding SEM-EDX elemental mapping of the selected area (f - i).

Fig. 2 shows the crystalline phases of undoped rGO/Co<sub>3</sub>O<sub>4</sub> (0%BGCO) composite and Bi-doped rGO/Co<sub>3</sub>O<sub>4</sub> nanohybrids obtained using the XRD. The diffraction peaks of rGO/Co<sub>3</sub>O<sub>4</sub> (0%BGCO) composite and Bi-doped rGO/Co<sub>3</sub>O<sub>4</sub> including 1%BGCO, 3%BGCO, and 6%BGCO nanohybrids are the same with those of the cubic Co<sub>3</sub>O<sub>4</sub> (JCPDS No. 43-1003). Due to the tiny doping amount of Bi sources in the preparation of Bi-doped rGO/Co<sub>3</sub>O<sub>4</sub> nanocomposite, no obviously crystalline phases corresponding to the Bi or Bi compound such as Bi<sub>2</sub>O<sub>3</sub> appeared in 1%BGCO, 3%BGCO, and 6%BGCO, which indicates that Bi doping did not obviously change the cubic structure of Co<sub>3</sub>O<sub>4</sub> (or that there are present below the minimum detection limit of XRD diffraction). On the other hand, the Bi<sub>2</sub>O<sub>3</sub> crystalline phase can be identified if the



doping amount of Bi is 10% in the 10%BGCO system (see Fig. S1, supporting information). Additionally, the diffraction peaks are sharp and strong, manifesting the good crystallinity and relatively small particle sizes, which are beneficial for the sensing performance [29].

**Fig. 2.** XRD patterns of 0%BGCO composite and BGCO nanohybrids of 1%BGCO, 3%BGCO and 6%BGCO.

Fig. 3a shows the high resolution XPS spectrum of C 1s, which indicates a high level oxidation of the graphene sheets, occurred during the exfoliation. There are three peaks with their binding energies at 284.2 eV, 286.1 eV and 289.7 eV, respectively, which can be assigned to the aromatic carbon (C-C), the epoxy or alkoxy (C-O) and the carbonyl carbon (C=O), respectively. Fig. 3b shows the deconvoluted O 1s spectrum of Bi-doped rGO/Co<sub>3</sub>O<sub>4</sub> composites. The two peaks centered at 529.7 and 531.6 eV are attributed to the O<sup>2-</sup> lattice oxygen, and chemisorbed oxygen species such as (O<sup>-</sup>, O<sub>2</sub><sup>-</sup> and O<sup>2-</sup>), respectively, leading to the formation of electron depletion layer within the matrix of 1%BGCO [44,45]. Fig. 3c shows the binding energies of Co 2p<sub>1/2</sub> and Co 2p<sub>3/2</sub> in Co 2p XPS spectra, which are located at 794.5 eV and 779.86 eV, respectively. The difference between these two binding energy values is ~14.6 eV, suggesting that both Co<sup>3+</sup> and Co<sup>2+</sup> are co-existed in the nanohybrids of 1%BGCO [46,8]. Moreover, the other two satellite peaks located at 796.6 eV and 781.6 eV are linked to the Co<sup>2+</sup> peak of two orbits [47]. Fig. 3d shows Bi 4f spectrum, and the binding energies for Bi 4f<sub>5/2</sub> and Bi 4f<sub>7/2</sub> are 164.90 and 159.56 eV, respectively. These show that all of the Bi species in the 1%BGCO sample are in the form of Bi<sup>3+</sup>, which agrees well with the previous reports [1,48]. Additionally, the high resolution XPS spectra of other three samples of 0%BGCO, 3%BGCO, and 6%BGCO were analyzed, revealing that the samples surface is composed of the elements of Co, C, O and Bi, in which Bi acts as a decorating component (see Fig. S2 to 4, supporting information).

**Fig. 3.** XPS spectra of Bi-doped rGO/Co<sub>3</sub>O<sub>4</sub> nanocomposites: (a) C 1s, (b) O 1s, (c) Co 2p and (d) Bi 4f, respectively.

Most of semiconductor-based sensors show temperature-dependent characteristics due to their unique electrical structures, which are strongly affected by temperature [49,50]. Thus, the different gas sensors have their individual optimum working temperatures. This is beneficial for improving the sensitivity and/or the selectivity according to the equation (1):

$$n_0 = 2(m_n^* k_0 T / 2\pi\hbar)^{3/2} \exp(-(E_c - E_f) / k_0 T) \quad (1) [1]$$

where  $T$  is Kelvin temperature scale,  $m_n^*$  is effective mass,  $k_0$  is the Boltzmann constant,  $\hbar$  is reduced Planck constant,  $E_c$  is the energy of conduction band bottom and  $E_f$  is the energy of Fermi level. We firstly tried to find the optimum operating temperature of the developed sensor. Fig. 4 shows the results of the sensing responses versus operating temperature ( $T$ ) of the 0%BGCO and Bi-doped rGO/Co<sub>3</sub>O<sub>4</sub> nanohybrids based sensor to 100 ppm ethanol. Through comparisons of the temperature dependent sensing characteristics in the temperature range of 80 - 200 °C, we found that the sensors of the 0%BGCO, 1%BGCO, 3%BGCO and 6%BGCO exhibit their optimum sensing properties at temperatures of 150 °C, 120 °C, 130 °C, and 140 °C, respectively. Obviously, the sensor of 1%BGCO exhibits the outstanding sensing performance among all the sensors, and its optimum working temperature is 120 °C.

**Fig. 4.** Sensing performances of the gas sensors toward 100 ppm ethanol gas at different operating temperatures.

To further reveal the changing trend of resistance ( $R_a$ ) for the different BGCO sensors, the relationship curves between  $R_a$  values and the proportion of Bi dopant at different operating temperature from 80 to 200 °C were obtained, and the results are shown in Fig. 5a. Obviously, the resistance values of 1%BGCO, 3%BGCO and 6%BGCO increase with the increase of Bi content in the BGCO nanohybrids at the same temperature, which indicates that the introduction of Bi element has significantly influenced the sensor's responses. The main reason can be ascribed to the fact that with a higher Bi content, the energy barrier and scattering cross-section could be increased, which would prevent the effective charge-transfer [51]. Additionally, the device's resistance decreases with the increase of the operating temperature, which is the

intrinsic characteristic of all the MOSCs. Furthermore, we also found that the resistance of 0%BGCO is the largest one among the samples of 1%BGCO, 3%BGCO and 6%BGCO. This phenomenon is in a good agreement with that reported in literature [39,52].

Fig. 5b exhibits the dynamic response and recovery characteristics of the sensors based on 1%BGCO and 0%BGCO to different ethanol concentrations from 500 ppb to 500 ppm tested at 120 °C. Obviously, the dynamic curves display a slow increase at a low ethanol concentration below 5 ppm. Afterwards the responses increase quickly after 5 ppm. In general, the 1%BGCO sensor exhibits much a higher response than that of 0%BGCO, which is mainly due to its increased content of Bi elements. Furthermore, the response of 1%BGCO sensor increases rapidly with the increasing concentration of ethanol, which can reach 178.1 at the ethanol concentration of 500 ppm. By taking the logarithm of  $R_a$  of samples of 0%BGCO and 1%BGCO, we found that the  $R_a$  of 1%BGCO exhibits a significant change with the increase of ethanol concentration, see Fig. 5c. On the other hand, it is worth mentioning that the  $R_a$  values of 1%BGCO, 3%BGCO, and 6%BGCO based sensors are much lower than that of 0%BGCO sensor due to the incorporation of Bi dopant, as shown in Fig 5d. Moreover, the resistance ( $R_a$ ) of all the sensors can return to the baseline level (see Fig. 5d) which manifest that the BGCO materials have excellent recovery property when exposed to fresh air again from the target gas of ethanol. The detailed response and recovery performance will be discussed in the following section of this study. For comparisons, the dynamic response and recovery curves of the sensors based on 3%BGCO and 6%BGCO are given in Figs. S4 and S5 (Supporting Information). Clearly, the response of 1%BGCO is 6.35, which is ~8.17 times as large as those of 3%BGCO and 6%BGCO, respectively. Furthermore, the response of 1%BGCO is gradually reaching to the saturation stage when the ethanol concentration is above 200 ppm, as shown in Fig. 5e. Table 1 summarizes the sensing data of ethanol using the 1%BGCO and 0%BGCO. According to the data in the table, the 1%BGCO sensor shows a superior response than that of 0%BGCO sensor, mainly because of its larger specific surface area (67.795 m<sup>2</sup>/g) and incorporation of Bi elements.

**Table 1** The response data of 1%BGCO and 0%BGCO based sensors toward 100 ppm ethanol at 120 °C.

Materials	Concentrations (unit: ppm)							
	0.5	1	5	20	50	100	200	500
1%BGCO	2.5	8.2	15.0	59.8	104.6	136.7	157.6	178.1
0%BGCO	1.2	1.2	1.4	1.6	1.7	2.0	2.2	2.4

Fig. 5f shows a typical repeatable sensing results of the 1%BGCO and 0%BGCO sensors after five cycles to 100 ppm of ethanol at 120 °C. It is indicated that both the 1%BGCO and 0%BGCO sensors show a good reproducibility after the cycling test, manifesting their good stabilities. However, the 0%BGCO sensor has only a very low sensitivity of 2.0 (see Table 1). Similarly, the cycling test results of dynamic responses of 3%BGCO and 6%BGCO to 100 ppm ethanol at 120 °C were also studied, and the results are shown in Figs. S6 and S7 (Supporting Information). Based on all these results, we can conclude that the introduction of Bi can significantly enhance the sensitivity of the rGO/Co<sub>3</sub>O<sub>4</sub> composite, meanwhile, the repeatability and stability of Bi-doped rGO/Co<sub>3</sub>O<sub>4</sub> nanohybrids are well maintained.

**Table 2** Gas sensing response values of various nanomaterials to ethanol gas.

Materials	Concn (ppm)	Temp (°C)	Response	Refs.
TiO <sub>2</sub> /Co <sub>3</sub> O <sub>4</sub>	100	160	65	[53]
ZnO-Co <sub>3</sub> O <sub>4</sub>	1000	200	106	[54]
Co <sub>3</sub> O <sub>4</sub> /Al <sub>2</sub> O <sub>3</sub>	50	240	8.9	[55]
Pd@Co <sub>3</sub> O <sub>4</sub> -ZnO	200	240	59	[56]
$\alpha$ -Bi <sub>2</sub> Mo <sub>3</sub> O <sub>12</sub> / Co <sub>3</sub> O <sub>4</sub>	100	170	30.25	[57]
rGO/CoTiO <sub>3</sub>	50	195	9	[58]
Co <sub>3</sub> O <sub>4</sub> /N-doped carbon foam	100	100	10.4	[59]
3 wt% rGO-Co <sub>3</sub> O <sub>4</sub>	100	180	13.5	[35]
rGO/Co <sub>3</sub> O <sub>4</sub>	100	200	21	[7]
Co <sub>3</sub> O <sub>4</sub> /N-RGO-0.5	100	200	24.5	[8]
1%BGCO	100	120	150	This work

**Fig. 5.** (a) The initial resistance alteration trend of the Bi-doped rGO/Co<sub>3</sub>O<sub>4</sub> (BGCO) nanohybrids induced by the proportion of Bi dopant at the different temperature from 80 to 200 °C; (b) Dynamic resistance changes of the 0%BGCO and 1%BGCO sensors when exposed to various ethanol gas toward 0.5-500 ppm ethanol at 120 °C, respectively; (c) Continuous resistance curves of the 0%BGCO and 1%BGCO sensors to various concentrations of ethanol at 120 °C; (d) The initial resistances ( $R_a$ ) of the 0%BGCO, 1%BGCO, 3%BGCO and 6%BGCO sensors varied with the ethanol concentration at 120 °C, respectively; (e) The response *vs* gas concentrations for 0%BGCO and 1%BGCO sensors, respectively; (f) Repeatability test of the 0%BGCO and 1%BGCO nanocomposite sensors to 100 ppm of ethanol at 120 °C.

Figs. 6a and b compare the response and recovery times of the 1%BGCO sensor and 0%BGCO sensor exposed to 100 ppm ethanol at 120 °C. The  $\tau_{res}$  of 0%BGCO sensor is 5 s, which is faster than that (89 s) of 1%BGCO sensor. On the other hand, both the sensors take a long time to recover 90% of its initial resistance, especially for the 1%BGCO (75 s). Most of the chemical sensors do not show good reversibility because the thermal energy is usually lower than the activation energy for desorption [60], which leads to a long  $\tau_{rec}$ . In addition, the gas sensor based on the rGO and its hybrids exhibits a much longer recovery time, which has often been reported in literature [61,62]. The main reason is attributed to the lamellar structure of rGO and mesoporous structures in 1%BGCO, which cause the slow diffusion of the ethanol molecules.

The long-term stability is also a very important parameter for gas sensors, thus the sensing stability of 1%BGCO and 0%BGCO exposed to 100 ppm ethanol was studied once per 10 days at 120 °C for a period of two months to evaluate their long-term stable performance. After two months, the 1%BGCO sensor still maintains 92% of the initial value with a good stability, but no clear change of the 0%BGCO because of its low sensitivity (Fig. 6c).

It is practical to investigate the sensing performance of the sensors at differently humid conditions because the humidity could greatly deteriorate the sensing property of gas sensors. This has been investigated and the obtained results are shown in Fig. 6d.

The responses are maintained at around 150 in the relative humidity range of 30-50 %, but then decreases gradually with the further increase of the relative humidity. The response can still retain at 101.8 when exposed to 100 ppm of ethanol as the relative humidity reaches to 80 %, indicating that the 1%BGCO sensor can work at a relatively high humidity up to 80% for the detection of ethanol.

**Fig. 6.** (a) and (b) Dynamic resistance curves of the 0%BGCO and 1%BGCO sensors toward 100 ppm ethanol at 120 °C; (c) Response stability of 0%BGCO and 1%BGCO sensors toward ethanol at 120 °C lasting for 10, 20, 30, 40, 50, and 60 days; (d) sensing performances of 0%BGCO and 1%BGCO sensors at different humidity with a concentration of 100 ppm ethanol gas 120 °C.

The selectivity and cross-responses of 0%BGCO and 1%BGCO sensors to different gases (all with a volume of 100 ppm) including acetone ( $\text{C}_2\text{H}_6\text{CO}$ ), isopropanol ( $(\text{CH}_3)_2\text{CHOH}$ ), benzene ( $\text{C}_6\text{H}_5\text{CH}_3$ ), ammonia ( $\text{NH}_3$ ), trimethylamine ( $\text{C}_3\text{H}_9\text{N}$ ) and  $\text{NO}_2$  were tested at 120 °C. The obtained results are shown in Fig. 7a, which clearly indicates that the gas sensors are more sensitive to ethanol than the other gases as well as oxidizing gas of  $\text{NO}_2$ , especially for 1%BGCO sensor (Fig. 7a). According to the literature [63], the incorporation of Bi dopant can promote the redox reaction, whereas the MOSCs can act as the catalyst. Therefore, the incorporation of Bi in BGCO provides the obtained sensing material with a superior catalytic selectivity for the redox reaction between chemisorbed oxygen and ethanol molecules.

It is well-known that gas sensing performance is related to surface chemisorption and catalytic reaction. The sensing mechanism based on the changes of conductivity is mainly originated from the interaction between the adsorbed gaseous molecules and sensing materials as well as the reactions between the absorbed target molecules and oxygen molecules on the surface of sensing material. Therefore, the sensing performance of MOSCs is closely related to their composition, electronic structure, crystallinity and crystal size, as well as surface morphology, which significantly affect their capacities of adsorbing target gas and oxygen ions on the surface. When the 1%BGCO sensor are exposed to air, oxygen molecules ( $\text{O}_2$ ) will be chemically

adsorbed onto the surface of the sensing materials to form oxygen ions ( $O^-$ ) through binding free hot electrons from the conductance band ( $E_c$ ) of 1%BGCO nanohybrids. The rGO nanosheets has a high electron mobility ( $\mu$ ), and could act as a medium to accept electrons. This facilitates the migration of carriers during the catalytic process, thus promoting the enhancement of sensing performances [31,32]. In this 1%BGCO nanohybrids system, when the sensing material was exposed to ethanol vapor gas, the ethanol molecules ( $CH_3CH_2OH$ ) can react with the adsorbed oxygen species on the surface. Thereafter, the electrons are released back to the  $E_c$  and thereby the sensor resistance is increased greatly.

To further study the electron transfer behavior in the 1%BGCO nanohybrid system, UPS analysis was carried out. As shown in Fig. 7b, the cut off energy of 1%BGCO nanohybrids is 16.93 eV, indicating that the work function of the 1%BGCO nanohybrids is 4.27 eV, which facilitates the transportation of electrons [64]. On the other hand, when the Bi-doped rGO/ $Co_3O_4$  nanohybrids are formed, conduction electrons of Bi-doped rGO grains are obtained from  $Co_3O_4$  (if holes, to follow the opposite direction) to balance Fermi level ( $E_f$ ), thus forming an electron depletion layer (EDL) at the interface Bi-doped rGO/ $Co_3O_4$  and consequently increasing the  $R_a$ , according to the energy band diagram as schematically illustrated in Figs. 7c and d. The processes can be expressed using the following two reactions (2) and (3): [65].

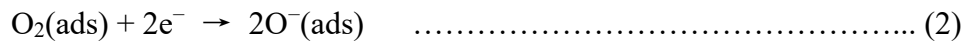


**Fig. 7.** (a) The selectivity of the sensors based on 0%BGCO and 1%BGCO to different gases with a concentration of 100 ppm at 120 °C; (b) UPS spectrum of 1%BGCO nanohybrids; (c) the energy band structure before contact of rGO and  $Co_3O_4$  and (d) the energy band structure after contact of rGO and  $Co_3O_4$ .

#### 4. Conclusions

In summary, the Bi-doped rGO/ $Co_3O_4$  (BGCO) nanohybrids have been rationally designed and successfully synthesized via one-step solvothermal process, and their

ethanol-sensing performances were investigated. Specifically, the 1%BGCO sensor shows the superior sensing response of 150 at 120 °C towards 100 ppm ethanol, a low detection limit (500 ppb). Moreover, the BGCO sensor shows excellent selectivity to ethanol compared to other organic volatile gases. The excellent gas sensing performance of 1%BGCO is mainly attributed to the appropriate content Bi and synergistic effect between Bi and rGO/Co<sub>3</sub>O<sub>4</sub> system. Additionally, incorporation of Bi dopant can promote the redox reaction, whereas the MOSCs act as the catalyst. Thus, this study provides a new strategy for using the Bi-doped rGO/Co<sub>3</sub>O<sub>4</sub> for ethanol sensing.

### **Acknowledgements**

This work was financially supported by the National Natural Science Foundation of China (Grant No. 51227804). This work was also funded by the Postdoctoral Scientific Research Foundation of Qingdao, National College Students Innovation and Entrepreneurship Training Program of China (No. G201911065028), College Students Innovation and Entrepreneurship Training Program of Qingdao University (X201911065058). The authors would like to thank the Chemical Experimental Teaching Center of Qingdao University for the characterizations, and Kehui Han from Shiyanjia Lab ([www.shiyanjia.com](http://www.shiyanjia.com)) for the XPS and UPS analysis.

### **Conflicts of interest**

There are no conflicts to declare

### **Note**

† These two authors contribute equally



## References

- [1] P. Wang, S.Z. Wang, Y.R. Kang, Z.S. Sun, X.D. Wang, Y. Meng, M.H. Hong, W.F. Xie, Cauliflower-shaped Bi<sub>2</sub>O<sub>3</sub>–ZnO heterojunction with superior sensing performance towards ethanol, *J. Alloys Compd.* 854 (2021), 157152.
- [2] X.Y. Tian, Z.Y. Liu, Z.W. Luo, X. Wu, F. Qiao, X.W. Wang, G.H. Li, J. Wu, J. Zhang, Z. Liu, J.H. Chu, Dual-mode sensor and actuator to learn human-hand tracking and grasping, *IEEE Trans. Electron Devices* 66 (2019) 5407–5410.
- [3] Z.W. Luo, X.T. Hu, X.Y. Tian, C. Luo, H.J. Xu, Q.L. Li, Q.H. Li, J. Zhang, F. Qiao, X. Wu, V.E. Borisenko, J.H. Chu, Structure-property relationships in graphene-based strain and pressure sensors for potential artificial intelligence applications, *Sensors* 19 (2019), 1250
- [4] J. Walker, P. Karnati, D.R. Miller, M. Al-Hashem, S.A. Akbar, P.A. Morris, A new open-access online database for resistive-type gas sensor properties and performance, *Sens. Actuators B Chem.* 321 (2020), 128591.
- [5] P. Srinivasan, A.J. Kulandaisamy, G.K. Mani, K.J. Babu, K. Tsuchiya, J.B.B. Rayappan, Development of an acetone sensor using nanostructured Co<sub>3</sub>O<sub>4</sub> thin films for exhaled breath analysis, *RSC Adv.* 9 (2019) 30226–30239.
- [6] F. Xing, S. Zhang, Y. Yang, W.S. Jiang, Z.B. Liu, S.W. Zhu, X.C. Yuan, Chemically modified graphene films for high-performance optical NO<sub>2</sub> sensors, *Analyst* 141 (2016) 4725–4732.
- [7] M.H. Tian, J.Y. Miao, P.F. Cheng, H.C. Mu, J.C. Tu, J.B. Sun, Layer-by-layer nanocomposites consisting of Co<sub>3</sub>O<sub>4</sub> and reduced graphene (rGO) nanosheets for high selectivity ethanol gas sensors, *Appl. Surf. Sci.* 479 (2019) 601–607.
- [8] G. Lin, H. Wang, X.Y. Lai, R.S. Yang, Y.Z. Zou, J.W. Wan, D. Liu, H. Jiang, Y. Hu, Co<sub>3</sub>O<sub>4</sub> /N-doped RGO nanocomposites derived from MOFs and their highly enhanced gas sensing performance, *Sens. Actuators B Chem.* 303 (2020), 127219
- [9] P.V. Shinde, N.M. Shinde, S.F. Shaikh, D. Lee, J.M. Yun, L.J. Woo, A.M. Al-Enizi, R.S. Mane, K.H. Kim, Room-temperature synthesis and CO<sub>2</sub>-gas sensitivity of bismuth oxide nanosensors, *RSC Adv.* 10 (2020) 17217–17227.

- [10] K. Kim, P.G. Choi, T. Itoh, Y. Masuda, Catalyst-free highly sensitive SnO<sub>2</sub> nanosheet gas sensors for parts per billion-level detection of acetone, *ACS Appl. Mater. Interfaces* 12 (2020) 51637–51644.
- [11] F.H. Zhang, Y.C. Wang, L. Wang, J. Liu, H.L. Ge, B. Wang, X.Y. Huang, X.D. Wang, Z.T. Chi, W.F. Xie, High performance In<sub>2</sub>(MoO<sub>4</sub>)<sub>3</sub>@In<sub>2</sub>O<sub>3</sub> nanocomposites gas sensor with long-term stability, *J. Alloys Compd.* 805 (2019) 180–188.
- [12] D. Wang, L.F. Deng, H.J. Cai, J.L. Yang, L.P. Bao, Y.H. Zhu, X.Y. Wang, Bimetallic PtCu nanocrystal sensitization WO<sub>3</sub> hollow spheres for highly efficient 3-Hydroxy-2-butanone biomarker detection, *ACS Appl. Mater. Interfaces* 12 (2020) 18904–18912.
- [13] N. Tammanoon, T. Iwamoto, T. Ueda, T. Hyodo, A. Wisitsoraat, C. Liewhiran, Y. Shimizu, Synergistic Effects of PdO<sub>x</sub>–CuO<sub>x</sub> Loadings on Methyl Mercaptan Sensing of Porous WO<sub>3</sub> Microspheres Prepared by Ultrasonic Spray Pyrolysis, *ACS Appl. Mater. Interfaces* 12 (2020) 41728–41739.
- [14] K.C. Wan, D. Wang, F. Wang, H.J. Li, J.C. Xu, X.Y. Wang, J.H. Yang, Hierarchical In<sub>2</sub>O<sub>3</sub>@SnO<sub>2</sub> core–shell nanofiber for high efficiency formaldehyde detection, *ACS Appl. Mater. Interfaces* 11 (2019) 45214–45225.
- [15] X. Wang, M.Z. Gao, Porous Co<sub>3</sub>O<sub>4</sub>/SnO<sub>2</sub> quantum dot (QD) heterostructures with abundant oxygen vacancies and Co<sup>2+</sup> ions for highly efficient gas sensing and oxygen evolution reaction, *Nanoscale* 10 (2018) 12045–12053.
- [16] P. Wang, S.Z. Wang, Q. Han, D.Q. Zou, W.K. Zhao, X.D. Wang, C. Luo, X. Yang, X. Wu, W.F. Xie, Construction of hierarchical  $\alpha$ -Fe<sub>2</sub>O<sub>3</sub>/SnO<sub>2</sub> nanoball arrays with superior acetone sensing performance, *Adv. Mater. Interfaces* (2020), 2001831.
- [17] N. Devabharathi, A.M. Umarji, S. Dasgupta, Fully inkjet-printed mesoporous SnO<sub>2</sub>-based ultrasensitive gas sensors for trace amount NO<sub>2</sub> detection, *ACS Appl. Mater. Interfaces* 12 (2020) 57207–57217.
- [18] Z.J. Han, Y. Qi, Z.Y. Yang, H.C. Han, Y.Y. Jiang, W.J. Du, X. Zhang, J.Z. Zhang, Z.F. Dai, L.L. Wu, C. Fletcher, Z. Wang, J.R. Liu, G.X. Lu, F.L. Wang, Recent advances and perspectives on constructing metal oxide semiconductor gas sensing materials for efficient formaldehyde detection, *J. Mater. Chem. C* 8 (2020) 13169–13188.

- [19] P. Karnati, S. Akbar, P.A. Morris, Conduction mechanisms in one dimensional core-shell nanostructures for gas sensing: A review, *Sens. Actuators B Chem.* 295 (2019) 127–143.
- [20] F.B. Gu, M.Y. Di, D.M. Han, S. Hong, Z.H. Wang, Atomically dispersed Au on  $\text{In}_2\text{O}_3$  nanosheets for highly sensitive and selective detection of formaldehyde, *ACS Sens.* 5 (2020) 2611–2619.
- [21] D. Wang, Y. Yin, P.C. Xu, F. Wang, P. Wang, J.C. Xu, X.Y. Wang, X.X. Li, The catalytic-induced sensing effect of triangular  $\text{CeO}_2$  nanoflakes for enhanced BTEX vapor detection with conventional ZnO gas sensors, *J. Mater. Chem. A* 8 (2020) 11188–11194.
- [22] H.Y. Tang, L.N. Sacco, S. Vollebregt, H.Y. Ye, X.J. Fan, G.Q. Zhang, Recent advances in 2D/nanostructured metal sulfide-based gas sensors: mechanisms, applications, and perspectives, *J. Mater. Chem. A* 8 (2020) 24943–24976.
- [23] A. Beniwal, Sunny,  $\text{SnO}_2\text{-ZnO-Fe}_2\text{O}_3$  tri-composite based room temperature operated dual behavior ammonia and ethanol sensor for ppb level detection, *Nanoscale* 12 (2020) 19732–19745.
- [24] Z.D. Hu, X.Y. Sun, H.F. Li, Y.R. Kang, X.Q. Song, P. Wang, Q.T. Luan, X.D. Wang, Z.T. Chi, W.F. Xie, Cobalt monosulfide nanofibers: ethanol sensing and magnetic properties, *Rare Metals* (2021).
- [25] Q.C. Li, D. Chen, J.M. Miao, S.J. Lin, Z.X. Yu, D.X. Cui, Z. Yang, X.P. Chen, Highly sensitive sensor based on ordered porous ZnO nanosheets for ethanol detecting application, *Sens. Actuators B Chem.* 326 (2021), 128952.
- [26] Z.J. Li, H. Li, Z.L. Wu, M.K. Wang, J.T. Luo, H. Torun, P.A. Hu, C. Yang, M. Grundmann, X.T. Liu, Y.Q. Fu, Advances in designs and mechanisms of semiconducting metal oxide nanostructures for high-precision gas sensors operated at room temperature, *Mater. Horizons* 6 (2019) 470–506.
- [27] I. Boehme, U. Weimar, N. Barsan, Unraveling the surface chemistry of CO sensing with  $\text{In}_2\text{O}_3$  based gas sensors, *Sens. Actuators B Chem.* 326 (2021), 129004.
- [28] V.S. Bhati, S. Ranwa, S. Rajamani, K. Kumari, R. Raliya, P. Biswas, M. Kumar, Improved sensitivity with low limit of detection of a hydrogen as sensor based on rGO-

loaded Ni-doped ZnO nanostructures, *ACS Appl. Mater. Interfaces* 10 (2018) 11116–11124.

[29] L.H. Liu, M. Yang, S. Gao, X.F. Zhang, X.L. Cheng, Y.M. Xu, H. Zhao, L.H. Huo, Z. Major,  $\text{Co}_3\text{O}_4$  hollow nanosphere-decorated graphene sheets for  $\text{H}_2\text{S}$  sensing near room temperature, *ACS Appl. Nano Mater.* 2 (2019) 5409–5419.

[30] D.F. Ma, Y.J. Su, T. Tian, H. Yin, C. Zou, T.T. Huo, N.T. Hu, Z. Yang, Y.F. Zhang, Multichannel room-temperature gas sensors based on magnetic-field-aligned 3D  $\text{Fe}_3\text{O}_4@\text{SiO}_2@\text{reduced}$  graphene oxide spheres, *ACS Appl. Mater. Interfaces* 12 (2020) 37418–37426.

[31] Q.Y. Li, Y. Shen, T. Li, M. Cao, F. Gu, L.J. Wang, Enhanced ethanol sensing performances of hetero-assembly  $\text{Zn}_{1-x}\text{Fe}_x\text{O}/\text{rGO}$  nanocomposites, *Sens. Actuators B Chem.* 314 (2020), 128032.

[32] N. Pienutsa, P. Roongruangsree, V. Seedokbuab, K. Yannawibut, C. Phatoomvijitwong, S. Srinives,  $\text{SnO}_2$ -graphene composite gas sensor for a room temperature detection of ethanol, *Nanotechnology* 32 (2020), 115502.

[33] M.A. Modenes-Junior, C.A. Zito, T.M. Perfecto, D.P. Volanti, Ethanol detection using composite based on reduced graphene oxide and CuO hierarchical structure under wet atmosphere, *Mater. Sci. Eng. B* 248 (2019), 114385.

[34] Z.L. Tang, X.C. Deng, Y. Zhang, X.D. Guo, J.Q. Yang, C.L. Zhu, J. Fan, Y.F. Shi, B.J. Qing, F.Y. Fan,  $\text{MoO}_3$  nanoflakes coupled reduced graphene oxide with enhanced ethanol sensing performance and mechanism, *Sens. Actuators B Chem.* 297 (2019), 126730.

[35] X.D. Liu, J.Y. Liu, Q. Liu, R.R. Chen, H.S. Zhang, J. Yu, D.L. Song, J.Q. Li, M.L. Zhang, J. Wang, Template-free synthesis of rGO decorated hollow  $\text{Co}_3\text{O}_4$  nano/microspheres for ethanol gas sensor, *Ceram. Int.* 44 (2018) 21091–21098.

[36] S. Syed Zahirullah, P. Immanuel, S. Pravinraj, P. Fermi Hilbert Inbaraj, J. Joseph Prince, Synthesis and characterization of Bi doped ZnO thin films using SILAR method for ethanol sensor, *Materials Letters* 230 (2018) 1–4.

[37] X. Li, D. Jiang, Y. Fan, N. Zhang, C. Liu, S. Adimi, J.R. Zhou, S.P. Wen, S.P. Ruan, The effects of Zr-doping on improving the sensitivity and selectivity of a one-

dimensional  $\alpha$ -MoO<sub>3</sub>-based xylene gas sensor, *Inorg. Chem. Front.* 7 (2020) 1704-1712.

[38] V.K. Tomer, S. Duhan, Correction: Ordered mesoporous Ag-doped TiO<sub>2</sub>/SnO<sub>2</sub> nanocomposite based highly sensitive and selective VOC sensors, *J. Mater. Chem. A* 8 (2020) 20189-20190.

[39] Q. Yang, Q.L. Wu, Y. Liu, S.P. Luo, X.T. Wu, X.X. Zhao, H.Y. Zou, B.H. Long, W. Chen, Y.J. Liao, L.X. Li, P.K. Shen, L.L. Duan, Z.W. Quan, Novel Bi-doped amorphous SnO<sub>x</sub> nanoshells for efficient electrochemical CO<sub>2</sub> reduction into formate at low overpotentials, *Adv. Mater.* 32 (2020), 2002822.

[40] P. Velusamy, R. Xing, R.R. Babu, E. Elangovan, J. Viegas, S. Liu, M.Sridaran, A study on formaldehyde gas sensing and optoelectronic properties of Bi-doped CdO thin films deposited by an economic solution process, *Sens. Actuators B Chem.* 297 (2019) 126718.

[41] Y.Y. Jian, W.W. Hu, Z.H. Zhao, P.F. Cheng, H. Haick, M.S. Yao, W.W. Wu, Gas sensors based on chemi-resistive hybrid functional nanomaterials, *Nano-Micro Letters* 12 (2020), 71.

[42] Y.F. Huang, W.C. Jiao, Z.M. Chu, G.M. Ding, M.L. Yan, X. Zhong, R.G. Wang, Ultrasensitive room temperature ppb-level NO<sub>2</sub> gas sensors based on SnS<sub>2</sub>/rGO nanohybrids with P–N transition and optoelectronic visible light enhancement performance, *J. Mater. Chem. C* 7 (2019) 8616-863625.

[43] J.Y. Zhang, Y. Yu, P. Wang, C. Luo, X. Wu, Z.Q. Sun, J.L. Wang, W.D. Hu, G.Z. Shen, Characterization of atomic defects on the photoluminescence in two-dimensional materials using transmission electron microscope, *InfoMat* 1 (2019) 85-97.

[44] T.J. Hsueh, S.S. Wu, Highly sensitive Co<sub>3</sub>O<sub>4</sub> nanoparticles/MEMS NO<sub>2</sub> gas sensor with the adsorption of the Au nanoparticles, *Sens. Actuators B Chem.* (2020) 129201.

[45] N. Jayababu, M. Poloju, J. Shruthi, M.V.R. Reddy, NiO decorated CeO<sub>2</sub> nanostructures as room temperature isopropanol gas sensors, *RSC Adv.* 9 (2019) 13765-13775.

[46] Q.X. Feng, X.G. Li, J. Wang, A.M. Gaskov, Reduced graphene oxide (rGO) encapsulated Co<sub>3</sub>O<sub>4</sub> composite nanofibers for highly selective ammonia sensors, *Sens. Actuators B Chem.* 222 (2016) 864-870.

- [47] J. Wu, Y. Yang, C.X. Zhang, H. Yu, L.C. Huang, X.T. Dong, J.X. Wang, X.L. Wang, Extremely sensitive and accurate H<sub>2</sub>S sensor at room temperature fabricated with In-doped Co<sub>3</sub>O<sub>4</sub> porous nanosheets, *Dalton Trans.* 48 (2019) 7720-7727.
- [48] P.V. Shinde, B.G. Ghule, N.M. Shinde, Q.X. Xia, S. Shaikh, A.V. Sarode, R.S. Mane, K.H. Kim, Room-temperature successive ion transfer chemical synthesis and the efficient acetone gas sensor and electrochemical energy storage applications of Bi<sub>2</sub>O<sub>3</sub> nanostructures, *New J. Chem.* 42 (2018) 12530-12538.
- [49] X.J. Yang, V. Salles, Y.V. Kaneti, M.S. Liu, M. Maillard, C. Journet, X.C. Jiang, A. Brioude, Fabrication of highly sensitive gas sensor based on Au functionalized WO<sub>3</sub> composite nanofibers by electrospinning, *Sens. Actuators B Chem.* 220 (2015) 1112-1119.
- [50] R.K. Mishra, G. Murali, T.H. Kim, J.H. Kim, Y.J. Lim, B.S. Kim, P. P. Sahayd, S.H. Lee, Nanocube In<sub>2</sub>O<sub>3</sub>@RGO heterostructure based gas sensor for acetone and formaldehyde detection, *RSC Adv.* 7 (2017) 38714-38724.
- [51] W.M.A. El Rouby, A.E.A. Aboubakr, M.D. Khan, A.A. Farghali, P. Millet, N. Revaprasadu, Synthesis and characterization of Bi-doped g-C<sub>3</sub>N<sub>4</sub> for photoelectrochemical water oxidation. *Sol. Energy* 211 (2020) 478-487.
- [52] M.C. Wu, J.S. Chih, W.K. Huang, Bismuth doping effect on TiO<sub>2</sub> nanofibres for morphological change and photocatalytic performance, *CrystEngComm* 16 (2014) 10692-10699.
- [53] L.Q. Zhang, Z.F. Gao, C. Liu, Y.H. Zhang, Z.Q. Tu, X.P. Yang, F. Yang, Z. Wen, L.P. Zhu, R. Liu, Y.F. Li, L.S. Cui, Synthesis of TiO<sub>2</sub> decorated Co<sub>3</sub>O<sub>4</sub> acicular nanowire arrays and their application as an ethanol sensor, *J. Mater. Chem. A* 3 (2015) 2794-2801.
- [54] Y. Xiong, W.W. Xu, Z.Y. Zhu, Q.Z. Xue, W.B. Lu, D.G. Ding, L. Zhu, ZIF-derived porous ZnO-Co<sub>3</sub>O<sub>4</sub> hollow polyhedrons heterostructure with highly enhanced ethanol detection performance, *Sens. Actuators B Chem.* 253 (2017) 523-532.
- [55] X. Wang, R.Y. Cao, S.W. Zhang, P.Y. Hou, R.X. Han, M.H. Shao, X.J. Xu, Hierarchical flowerlike metal/metal oxide nanostructures derived from layered double hydroxides for catalysis and gas sensing, *J. Mater. Chem. A* 5 (2017) 23999-24010.

- [56] Y.J. Sun, Z.P. Wang, W.D. Wang, G. Li, P.W. Li, K. Lian, W.D. Zhang, S. Zhuiykov, J. Hu, L. Chen, Electrospinning preparation of Pd@Co<sub>3</sub>O<sub>4</sub>-ZnO composite nanofibers and their highly enhanced VOC sensing properties, Mater. Res. Bull. 109 (2019) 255–264.
- [57] S.U. Din, M.U. Haq, R. Khatoon, X. Chen, L. Li, M. Zhang, L. Zhu, A novel ethanol gas sensor based on  $\alpha$ -Bi<sub>2</sub>Mo<sub>3</sub>O<sub>12</sub>/Co<sub>3</sub>O<sub>4</sub> nanotube-decorated particles, RSC Adv. 10 (2020) 21940–21953.
- [58] J. Lu, N. Jia, L. Cheng, K.Y. Liang, J.F. Huang, J.Y. Li, rGO/CoTiO<sub>3</sub> nanocomposite with enhanced gas sensing performance at low working temperature, J. Alloys Compd. 739 (2018) 227–234.
- [59] L. Li, C. Zhang, R. Zhang, X. Gao, S. He, M. Liu, X. Li, W. Chen, 2D ultrathin Co<sub>3</sub>O<sub>4</sub> nanosheet array deposited on 3D carbon foam for enhanced ethanol gas sensing application, Sens. Actuators B Chem. (2017) 664–672.
- [60] A. Bag, N.E. Lee, Gas sensing with heterostructures based on two-dimensional nanostructured materials: a review, J. Mater. Chem. C 7 (2019) 13367–13383.
- [61] B. Wang, X.L. Wang, X.C. Li, Z.J. Guo, X. Zhou, Y.Q. Wu, The effects of amino substituents on the enhanced ammonia sensing performance of PcCo/rGO hybrids, RSC Adv. 8 (2018) 41280–41287.
- [62] H.F. Du, G.Z. Xie, Q.P. Zhang, Enhanced room temperature NO<sub>2</sub> sensing performance of RGO nanosheets by building RGO/SnO<sub>2</sub> nanocomposite system, Sensors 19 (2019), 4650.
- [63] Z.H. Tao, Y.W. Li, B. Zhang, G. Sun, J.L. Cao, Y. Wang, Bi-doped urchin-like In<sub>2</sub>O<sub>3</sub> hollow spheres: Synthesis and improved gas sensing and visible-light photocatalytic properties, Sens. Actuators B Chem. 321 (2020), 128623.
- [64] X.Y. Kou, F.Q. Meng, K. C, T.S. Wang, P. Sun, F.M. Liu, X. Yan, Y.F. Sun, F.M. Liu, K. Shimano, G.Y. Lu, High-performance acetone gas sensor based on Ru-doped SnO<sub>2</sub> nanofibers, Sens. Actuators B Chem. 320 (2020), 128292.
- [65] F. Wu, Q. Li, P. Wang, H. Xia, Z. Wang, Y. Wang, M. Luo, L. Chen, F.S. Chen, J.S. Miao, X.S. Chen, W. Lu, C.X. Shan, A.L. Pan, X. Wu, W.C. Ren, D. Jariwala, W.D. Hu, High efficiency and fast van der Waals hetero-photodiodes with a unilateral depletion

region, Nat. Commun. 10 (2019), 4663.

**Fig. 1.** (a) Illustration of the synthesis process of flower shaped Bi-doped rGO/Co<sub>3</sub>O<sub>4</sub> nanohybrids; (b) low-magnification SEM and (c) high-magnification SEM of Bi-doped rGO/Co<sub>3</sub>O<sub>4</sub> nanohybrids; (d) low-magnification TEM and (e) HR-TEM image of Bi-doped rGO/Co<sub>3</sub>O<sub>4</sub> nanohybrids; the corresponding SEM-EDX elemental mapping of the selected area (f - i).

**Fig. 2.** XRD patterns of 0%BGCO composite and BGCO nanohybrids of 1%BGCO, 3%BGCO and 6%BGCO.

**Fig. 3.** XPS spectra of Bi-doped rGO/Co<sub>3</sub>O<sub>4</sub> nanocomposites: (a) C 1s, (b) O 1s, (c) Co 2p and (d) Bi 4f, respectively.

**Fig. 4.** Sensing performances of the gas sensors toward 100 ppm ethanol gas at different operating temperatures.

**Fig. 5.** (a) The initial resistance alteration trend of the Bi-doped rGO/Co<sub>3</sub>O<sub>4</sub> (BGCO) nanohybrids induced by the proportion of Bi dopant at the different temperature from 80 to 200 °C; (b) Dynamic resistance changes of the 0%BGCO and 1%BGCO sensors when exposed to various ethanol gas toward 0.5-500 ppm ethanol at 120 °C, respectively; (c) Continuous resistance curves of the 0%BGCO and 1%BGCO sensors to various concentrations of ethanol at 120 °C; (d) The initial resistances ( $R_a$ ) of the 0%BGCO, 1%BGCO, 3%BGCO and 6%BGCO sensors varied with the ethanol concentration at 120 °C, respectively; (e) The response vs gas concentrations for 0%BGCO and 1%BGCO sensors, respectively; (f) Repeatability test of the 0%BGCO and 1%BGCO nanocomposite sensors to 100 ppm of ethanol at 120 °C.

**Fig. 6.** (a) and (b) Dynamic resistance curves of the 0%BGCO and 1%BGCO sensors toward 100 ppm ethanol at 120 °C; (c) Response stability of 0%BGCO and 1%BGCO sensors toward ethanol at 120 °C lasting for 10, 20, 30, 40, 50, and 60 days; (d) sensing performances of 0%BGCO and 1%BGCO sensors at different humidity with a



concentration of 100 ppm ethanol gas 120 °C.

**Fig. 7.** (a) The selectivity of the sensors based on 0%BGCO and 1%BGCO to different gases with a concentration of 100 ppm at 120 °C; (b) UPS spectrum of 1%BGCO nanohybrids; (c) the energy band structure before contact of rGO and Co<sub>3</sub>O<sub>4</sub> and (d) the energy band structure after contact of rGO and Co<sub>3</sub>O<sub>4</sub>.